Pergamon

Int. J. Heat Mass Transfer. Vol. 40, No. 8, pp. 1895–1905, 1997

0017–9310/97 $17.00+0.00

PII: S0017–9310(96)00223–2

Energy absorption in a conical cavity truncated by spherical cap subject to a focused high-intensity beam

C. Y. HO and P. S. WEI†

Institute of Mechanical Engineering, National Sun Yat-Sen University, Kaohsiung, Taiwan, Republic of China

(*Received* 14 *February* 1996 *and in final form* 7 *June* 1996)

Abstract—Energy absorption of a conical cavity truncated by a spherical cap subject to a focused beam is systematically and quantitatively investigated. The incident flux on any transverse cross-section has a Gaussian distribution, which is specified by the convergence angle, energy distribution parameter at the focal spot, and focal spot location relative to the workpiece surface. Absorption and scattering within the plasma in the cavity are assumed to be negligible. By accounting for specular and diffuse reflections the results show the effects of the spherical cap and cone angles of the cavity, locations and sizes of the focal spot, and convergence angles of the energy-beam on absorption. Asymptotic results agree with available solutions of simple models. An explanation for the occurrence of spiking in welding is also proposed.

1. INTRODUCTION

A deep and narrow vapor-filled cavity can be readily produced by using a focused high-intensity plasma arc, laser or electron beam [1, 2] in welding, drilling and cutting. The intensity of the beam is practically achieved by adjusting the focus current in an electron beam welder, as well as the distance between the energy source and surface of the workpiece. Focusing characteristics have been shown to have a strong influence on welding. Konkol *et al.* [3] observed that as the focal spot of an electron-beam was lowered from above the workpiece surface to below the surface, vertical cross-sections were changed from convex to parallel-sided to V-shaped. Spiking which refers to non-uniformity in depth or spacing was pronounced at the bottom of V-shaped fusion zones. Intensity of the incident flux was a cause of spiking, as investigated by Armstrong [4] and Giedt [5]. The focal spot location is also responsible for shrinkage cavities and the abnormally expanded fusion zone at the middle portion of deep penetration, as proposed and observed by Schiller *et al.* [6] and Irie *et al.* [7], respectively.

In realistic welding and drilling two important factors should be taken into account, namely the beam focusing characteristics and reflections of the cavity wall. Adams [8, 9] observed that the maximum joint penetration was achieved with the beam focused about 2.54 cm below the surface of a stainless steel in low- and high-voltage electron-beam welding. The sensitivity of the depth/width ratio increased with distance from the focus coil to the workpiece. These trends are consistent with results presented by Engquist [10], who emphasized that a small error in the focus current can result in a significant change in the focal spot location and that it is was best to operate at the shortest possible focus coil-to-workpiece distance.

Wei and Chow [11] theoretically verified the effects of beam focusing characteristics including the convergence angle, energy distribution parameter at the focal spot and location of the focal spot from the workpiece surface in high-power-density-beam welding. It was found that adjusting the focal spot at the workpiece surface is necessary to produce a uniform depth of the cavity or fusion zone. Irrespective of the convergence angle, the depth of the cavity is then determined by the energy distribution parameter at the workpiece surface. The abnormally expanded fusion zone, however, was not obtained. This defect may result from specular reflections of the incident flux.

The significant effect of reflections on high-intensity beam drilling was experimentally examined by Arata [12] by heating two acrylic plates separated by different distances. Cavities were produced in both the top and bottom workpieces. In view of energy reflections by walls, an increase in the gap between workpieces resulted in the opening diameter of the cavity in the bottom workpiece being much larger than the cavity diameter at the bottom surface of the top workpiece.

The distribution of energy absorbed by the cavity where reflections are accounted for is quite different from the incident flux. Assuming that absorption within the ionized vapor or plasma is negligible and using a Monte-Carlo method [13]–[16] Wang and Wei [17] found that energy absorbed by the cavity of a paraboloid of revolution subject to a collimated par-

† Author to whom correspondence should be addressed.

NOMENCLATURE

dA	elemental area on cavity wall, as illustrated in Fig. 2
A_n	cross-sectional area of beam, defined by equation (3)
f	focal spot location $= \hat{f}/\hat{r}_0$, as shown in Fig. 2
dF	differential view factor
g	function defined by equation (9)
h	cavity depth, $\hat{h}/\hat{r}_0$, as shown in Fig. 2
q	incident flux $= \hat{q}\hat{r}_0^2/\hat{Q}$, as defined in equation (1)
$\hat{Q}$	beam power
q_w	dimensionless energy flux absorbed by cavity wall, $\hat{q}_w\hat{r}_0^2/\hat{Q}$
r	radial coordinate, $\hat{r}/\hat{r}_0$
r_c	spherical cap radius
r_f	focal spot size, $\hat{r}_f/\hat{r}_0$, as shown in Fig. 2
r_p	radius of curvature for spherical cap
$\hat{r}_0$	dimensional cavity opening radius
r_s	critical radius
s	distance, as shown in Fig. 2
s_0	$r_f/\tan\beta + \text{sign}(f+h)(f+h)$
W	diffuse radiosity
z	vertical coordinate, $z = \hat{z}/\hat{r}_0$, as shown in Fig. 2.

Greek symbols

α	absorptivity
β	half convergence angle
β'	incident angle
η	surface coordinate, as illustrated in Fig. 2
θ	angle, as illustrated in Fig. 3
ρ_d, ρ_s	diffuse and specular reflectivity
ϕ	half cone angle, as illustrated in Fig. 2
ψ	angle, as illustrated in Fig. 2
ω	azimuth angle, as illustrated in Fig. 2.

Superscript

$\wedge$	dimensional quantity.

Subscripts

i, j	emitting and receiving point
jn	the first striking point of n times specular reflections received at point j
m, n	mth and nth striking point
t	total
0	point source or cavity opening
1, 2	the first and second striking point.

allel beam of Gaussian and uniform distributions exhibits distinct regions determined by dimensionless radii r_s. When radii are smaller than this critical radius the wall is irradiated primarily by a direct incident energy-beam, after the first specular reflection energy rays have escaped to the surroundings. In the other region where the radii are greater than the critical radius, the wall experiences the first specularly reflected rays from itself in addition to the direct incident energy. A jump in absorption which can be a hundred times the incident flux therefore occurs near the critical radius.

This work is an extension of the study reported by Wang and Wei [17]. The cavity, however, is considered to be a cone truncated by a spherical cap. Not only specular and diffuse reflections by the wall but also the beam focusing characteristics are accounted for. A more relevant energy transport to the workpieces is therefore determined.

2. SYSTEM MODEL AND ANALYSIS

As illustrated in Fig. 1, a focused incident flux on a conical cavity truncated by a spherical cap is partially absorbed and the remainder specularly and diffusely reflected. The half angle of the conical cavity is ϕ, while the radius of the spherical cap is r_c, as shown in Fig. 2. The displacement of the focal spot from the workpiece surface is denoted by f being positive if above the surface and negative if below. The size of the focal spot and convergence angle are r_f and 2β, respectively. The incident flux with the focal spot above the cavity base can be considered as emitted by a virtual point source. When the focal spot lies below the cavity base the energy is emitted by an imaged point source. The sources are located at $\mathbf{r}_0 = \text{sign}(f+h)[s_0 - r_p(1-\cos\phi)\,\text{sign}(f+h)]\mathbf{k}$ where the function $\text{sign}(f+h) \equiv (f+h)/|f+h| = +1$ or -1 denotes a focal spot lying above or below the cavity base, respectively. The primary assumptions made are the following:

(1) The incident flux has a Gaussian distribution at any transverse cross-section. This was confirmed by Hicken *et al.* [18] by measuring distributions of the incident flux at vertical distances within about 0.635 cm from the focal spot of an electron-beam. As for a laser-beam the Gaussian distribution is valid for the spatially coherent TEM_{00} model.

(2) The cavity is idealized by a conical cone truncated by a spherical cap to a first approximation. In reality, the cavity can be a cone, paraboloid of revolution, or other irregular geometries during welding or drilling. It also becomes slightly asymmetric in a moving heat source [19]. The cavity, however, was roughly observed to be approximately conical and truncated by a spherical cap near the cavity base [20].

(3) The cavity is considered to be stationary even

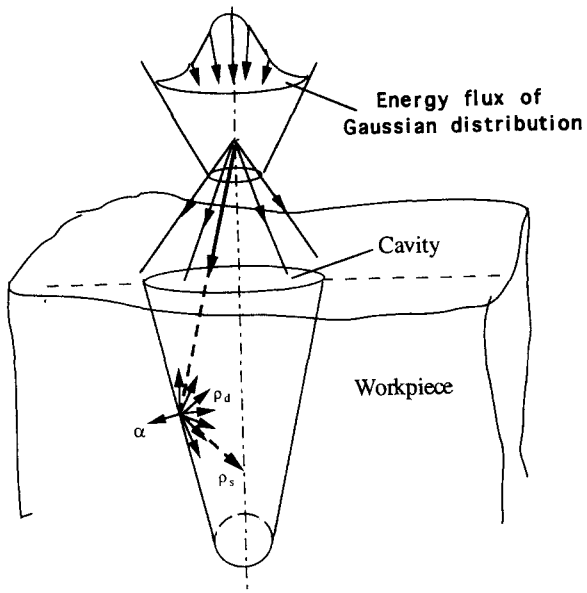

Fig. 1. Sketch indicating energy absorbed and reflected specularly and diffusely in a conical cavity with a spherical cap produced by a focused beam.

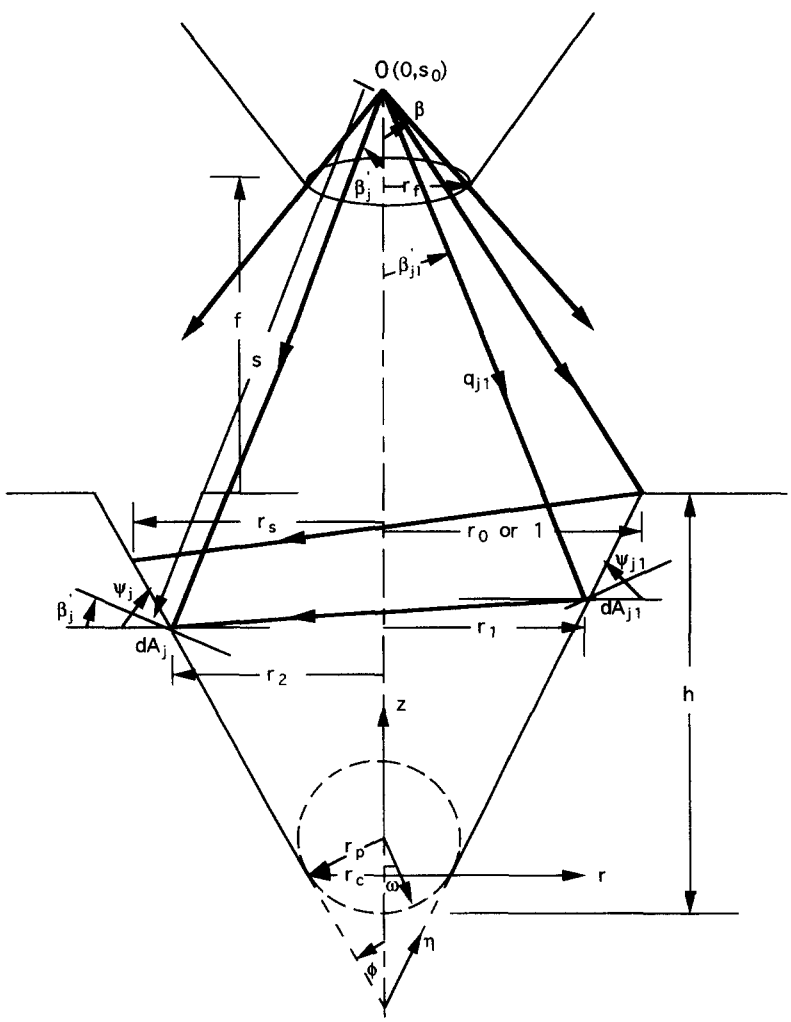

Fig. 2. Physical model and coordinate system.

though drilling and welding are unsteady. This is because the time scale for energy redistribution can be estimated to be around 10^{-10}s, which is much smaller than 10^{-3} s for drilling a cavity, as measured by von Allmen [21] and Miyazaki [22].

(4) The cavity is a specular and diffuse reflector. In reality, the cavity wall is not smooth. In order to simplify the problem without loss of generality, the surface is modeled by choosing appropriate values of specular and diffuse reflectivities. Radiative properties are independent of direction and wavelength of the incident energy-beam.

(5) Absorption within the plasma in the cavity is ignored. Temperatures and concentrations of electrons in iron plasmas during deep welding with a continuous CO_2 laser were measured by Poueyo-Verwaerde *et al.* [23] and Collur and DebRoy [24] for temperature as high as 7000K and densities up to 9×10^{23} particles/m^3. The absorption length due to electron-neutral interactions for these conditions is 0.25 m while that resulting from electron-ionized iron is 0.03 m. As a consequence, $80\%\pm10\%$ of a beam power of 15 kW and $92\%\pm5\%$ of 1 kW beam power are transmitted. Lengths of inverse Brehmstrahlung absorption [25] were similarly found to be 1 m for plasmas of aluminum and titanium irradiated by a continuous CO_2 laser [26] and pulsed YAG laser [27], respectively.

(6) Radiation in the plasma is neglected. Shui *et al.* [26] calculated emission from a layer of vapor over aluminum. Emission due to free-bound transitions, which are dominant in plasmas, was less than 5×10^8 W m^{-2} for temperatures below 10 000K and vapor densities around 10^{25} particle/m^3. Radiation from the plasma thus is only of the order of 1% of the incident flux.

(7) Scattering between the incident flux and ultra fine particles resulting from aggregates formed from the vapor or blown off the liquid layer at the cavity wall is neglected. Energy losses due to Rayleigh scattering are inversely proportional to the fourth power of wavelength of the incident flux [27]. Matsunawa and Ohnawa [27] and Matsunawa *et al.* [28] also experimentally confirmed a great reduction of the scattered intensity at lower ambient pressure. Since the average size of particles was around 10^{-9} m (and decreased with the ambient pressure) [27, 28] and the temperature was low, attenuation due to Rayleigh scattering for a YAG or CO_2 laser is less than inverse bremsstrahlung absorption. The Mie scattering can also be ignored because energy losses are dependent on the sixth power of the size of particles [29]. A typical value of the absorption length due to the Mie scattering was around 0.01 m, as estimated by Miyamoto *et al.* [30]. In general, the plasma can be considered as a transparent medium under working conditions such as produced by an electron-beam heat source [29], an energy-beam with a short wavelength (e.g. Nd : YAG laser), low surrounding pressure, and vapor having a low ionization threshold.

(8) The effects of the refraction on the energy-beam are ignored. Although this is relevant for a Nd : YAG laser, it is negligible since the refractive index decreases with λ^2 [23].

2.1. *Radiant exchange equation*

With the above assumptions, irradiation on the cavity wall at a given angle β_j' is

$$W(\beta_j') = \rho_d \left\{ q_j \cos\left[\psi_j - \beta_j' \operatorname{sign}(f+h)\right] + \int W(\beta_i')\, \mathrm{d}F_{(\mathrm{d}A_j - \mathrm{d}A_i)} + \sum_{n=1}^{\infty} \rho_s^n q_{jn} \cos\left[\psi_{jn} - \beta_{jn}' \operatorname{sign}(f+h)\right] \frac{\mathrm{d}A_{jn}}{\mathrm{d}A_j} \right\} \quad (1)$$

where the first term on the right-hand side represents the radiation directly arriving at $\mathrm{d}A_j$ from outside the cavity through its opening, the integral term gives the diffuse irradiation received by $\mathrm{d}A_j$ from the entire surface of the cavity, and the summation term is the energy received by the element $\mathrm{d}A_j$ which has undergone only specular reflections on the cavity surface before reaching $\mathrm{d}A_j$.

2.2. *Focused incident flux*

The focused incident flux of a Gaussian distribution is represented by

$$q_j = \frac{3}{A_n} \exp\left[-3 \left(\frac{\beta_j'}{\beta} \right)^2 \right] \quad (2)$$

where the area of any transverse cross-section of the beam is expressed by

$$A_n = 2\pi s^2 (1 - \cos\beta). \quad (3)$$

In equation (3) the distance between the point source and striking point of the incident ray on the cavity wall is (see Fig. 2)

$$s(\omega_j, z_j) = \sqrt{\left\{ s_0 - \left[r_p (1 - \cos\omega_j) + z_j \right] \operatorname{sign}(f+h) \right\}^2 + (r_p \sin\omega_j + z_j \tan\phi)^2} \quad (4)$$

where the vertical coordinate z is set to be zero for the incident energy ray impinging on the spherical cap, while the angle $\omega_j = 90^\circ - \phi$ on the conical wall. The incident angle in equation (2) is

$$\beta_j'(\omega_j, z_j) = \tan^{-1} \left\{ \frac{r_p \sin\omega_j + z_j \tan\phi}{s_0 - \left[r_p (1 - \cos\omega_j) + z_j \right] \operatorname{sign}(f+h)} \right\}. \quad (5)$$

The inclination angles of the wall (see Fig. 2) in equation (1) are

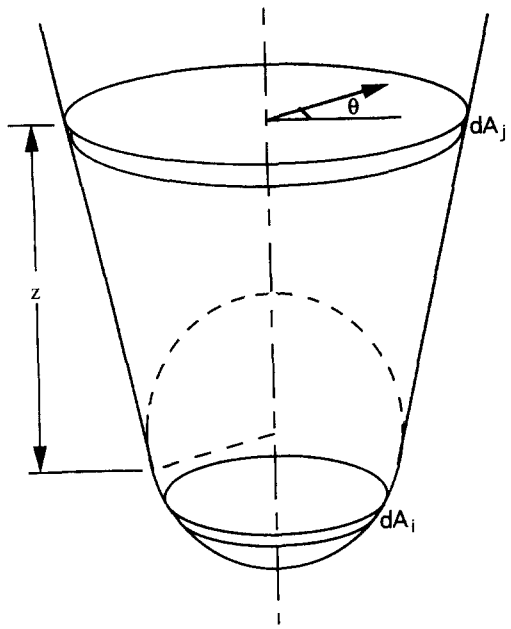

Fig. 3. Geometry for view factor.

$$\psi_j(\omega_j, z_j) = \begin{cases} 90^\circ - \phi & z_j > 0 \quad \text{for conical wall} \\ \sin^{-1}\left(\dfrac{s \sin \beta_j'}{r_p}\right) & z_j \leqslant 0 \quad \text{for spherical cap} \end{cases} \tag{6}$$

2.3. *The total view factor*

The differential view factor between two parallel rings on the cavity wall, as illustrated in Fig. 3, is [31]

$$dF_{dA_i - dA_j} = \frac{dA_j \cos\phi}{8\pi r_p^2 \left(\cos\phi + \dfrac{z_j}{r_p}\tan\phi\right)\sin\omega_i} \times \left(2\sin\omega_i + r_p \left.\frac{\partial^2 g}{\partial z\, \partial\omega}\right|_{z_j,\omega_i}\right) \tag{7}$$

or

$$dF_{dA_j - dA_i} = \frac{dA_i \cos\phi}{8\pi r_p^2 \left(\cos\phi + \dfrac{z_j}{r_p}\tan\phi\right)\sin\omega_i} \times \left(2\sin\omega_i + r_p \left.\frac{\partial^2 g}{\partial z\, \partial\omega}\right|_{z_j,\omega_i}\right) \tag{8}$$

where the function g is given by

$$g(\omega, z) = \left\{\left[\left(\frac{z}{r_p} + \cos\omega - \sin\phi\right)^2 + \left(\cos\phi + \frac{z}{r_p}\tan\phi\right)^2 + \sin^2\omega\right]^2 - \left[2\sin\omega\left(\cos\phi + \frac{z}{r_p}\tan\phi\right)\right]^2\right\}^{1/2}. \tag{9}$$

Using the law of coplanarity and the law of reflection a relationship between the originating, reflecting, and receiving points on the wall yields

$$\begin{aligned} &\left[\left(\sin\omega_m + \frac{z_m}{r_p}\cos\phi\right)\left(\sin\omega_m + \frac{z_m}{r_p}\tan\phi\right)\right. \\ &\quad - \left(\sin\omega_{m-1} + \frac{z_{m-1}}{r_p}\tan\phi\right)\left(\sin\omega_m + \frac{z_m}{r_p}\cos\phi\right) \\ &\quad \cdot\cos(\theta_m - \theta_{m-1}) + \left(\cos\omega_m + \frac{z_m}{r_p}\sin\phi\right) \\ &\quad \left.\left(\cos\omega_m - \cos\omega_{m-1} + \frac{z_{m-1}}{r_p} - \frac{z_m}{r_p}\right)\right] \\ &\quad \cdot\left[\left(\sin\omega_{m-1} + \frac{z_{m-1}}{r_p}\tan\phi\right)^2 + \left(\sin\omega_m\right.\right. \\ &\quad \left.\left. + \frac{z_m}{r_p}\tan\phi\right)^2 - 2\left(\sin\omega_{m-1} + \frac{z_{m-1}}{r_p}\tan\phi\right)\right. \\ &\quad \cdot\left(\sin\omega_m + \frac{z_m}{r_p}\tan\phi\right)\cos(\theta_m - \theta_{m-1}) \\ &\quad \left. + \left(\cos\omega_m - \cos\omega_{m-1} + \frac{z_{m-1}}{r_p} - \frac{z_m}{r_p}\right)^2\right]^{-1/2} \\ &= \left[\left(\sin\omega_m + \frac{z_m}{r_p}\cos\phi\right)\left(\sin\omega_m + \frac{z_m}{r_p}\tan\phi\right)\right. \\ &\quad - \left(\sin\omega_{m+1} + \frac{z_{m+1}}{r_p}\tan\phi\right)\left(\sin\omega_m + \frac{z_m}{r_p}\cos\phi\right) \\ &\quad \cdot\cos(\theta_{m+1} - \theta_m) + \left(\cos\omega_m + \frac{z_m}{r_p}\sin\phi\right) \\ &\quad \left.\cdot\left(\cos\omega_m - \cos\omega_{m+1} + \frac{z_{m+1}}{r_p} - \frac{z_m}{r_p}\right)\right] \\ &\quad \cdot\left[\left(\sin\omega_m + \frac{z_m}{r_p}\tan\phi\right)^2 + \left(\sin\omega_{m+1}\right.\right. \\ &\quad \left.\left. + \frac{z_{m+1}}{r_p}\tan\phi\right)^2 - 2\left(\sin\omega_{m+1} + \frac{z_{m+1}}{r_p}\tan\phi\right)\right. \\ &\quad \cdot\left(\sin\omega_m + \frac{z_m}{r_p}\tan\phi\right)\cos(\theta_{m+1} - \theta_m) \\ &\quad \left. + \left(\cos\omega_m - \cos\omega_{m+1} + \frac{z_{m+1}}{r_p} - \frac{z_m}{r_p}\right)^2\right]^{-1/2} \end{aligned} \tag{10}$$

and for an axisymmetric case [32]

$$\theta_{m+1} - \theta_m = \theta_m - \theta_{m-1} \equiv \Delta\theta. \tag{11}$$

Equations (10) and (11) involve different relationships for locations of the originating, reflecting, and receiving points on the cone and spherical cap. They are (a) cone–cone–cone; (b) cone–cone–cap; (c) cone–cap–cone; (d) cone–cap–cap; (e) cap–cone–cone; (f) cap–

cone–cap; (g) cap–cap–cone; (h) cap–cap–cap. Cases (a) and (h) are specially considered below.

2.3.1. *Specular reflections in cone–cone–cone.* When any three points on the conical wall have the same angles $\omega_{m-1} = \omega_m = \omega_{m+1} = 90° - \phi$, where $m \geqslant 2$. Equation (10) then reduces to

$$[1-\cos(\theta_{m-1}-\theta_m)]\left\{1+\left(\frac{\eta_m}{\eta_{m-1}}\right)^2 - \frac{2\eta_m}{\eta_{m-1}}[\sin^2\phi\cos(\theta_{m-1}-\theta_m)+\cos^2\phi)]\right\}^{-1/2} = [1-\cos(\theta_{m+1}-\theta_m)]\left\{1+\left(\frac{\eta_m}{\eta_{m+1}}\right)^2 - \frac{2\eta_m}{\eta_{m+1}}[\sin^2\phi\cos(\theta_{m+1}-\theta_m)+\cos^2\phi)]\right\}^{-1/2} \tag{12}$$

where the surface coordinate η is satisfied by

$$\eta\sin\phi = r_p\cos\phi + z\tan\phi. \tag{13}$$

A substitution of equation (11) into equation (12) gives

$$\frac{\eta_m}{\eta_{m+1}} + \frac{\eta_m}{\eta_{m-1}} = 2-2(1-\cos\Delta\theta)\sin^2\phi \equiv K \tag{14}$$

where $\Delta\theta = 180°$ due to the axisymmetric system. Combining all equations for $m = 2, \ldots, n-1$, a relationship between points 1, 2, and n is found [32]

$$\eta_2 = \frac{C_{n-1}\eta_1\eta_n}{C_{n-2}\eta_n+\eta_1}, \quad n \geqslant 2. \tag{15}$$

The coefficients in equation (15) are

$$C_n = \sum_{t=0}^{I}\frac{(-1)^t}{t!}K^{n-1-2t}\prod_{s=1}^{s=t}[n-(t+s)] \tag{16}$$

where I is the integer part of $(n-1)/2$.

2.3.2. *Specular reflections in cap–cap–cap.* For any three points on the spherical cap, $z_{m-1} = z_m = z_{m+1} = 0$, $m \geqslant 2$. Equations (10) and (11) then give $\omega_{m+1} - \omega_m = \omega_m - \omega_{m-1}$, which leads to

$$\omega_2 = \omega_1 + \frac{\omega_n - \omega_1}{n-1}, \quad n \geqslant 2. \tag{17}$$

Substituting equations (15), (17) and (10) into equation (8) the total view factor for other cases can be determined [32].

2.4. *Specular reflection*

Specular reflections of an energy ray emitted from the virtual or imaged point source are governed by the laws of coplanarity and reflection. That is,

$$\frac{(\mathbf{r}_0-\mathbf{r}_1)\,\mathrm{sign}(f+h)\cdot\mathbf{n}_1}{|(\mathbf{r}_0-\mathbf{r}_1)\,\mathrm{sign}(f+h)\cdot\mathbf{n}_1|} = \frac{(\mathbf{r}_2-\mathbf{r}_1)\cdot\mathbf{n}_1}{|\mathbf{r}_2-\mathbf{r}_1|} \tag{18}$$

where $\mathbf{r}_0$, $\mathbf{r}_1$ and $\mathbf{r}_2$ are position vectors of the point source, the first and second striking points, respectively. The polar angles for axisymmetric case are satisfied by

$$\theta_2 - \theta_1 = \theta_1 - \theta_0. \tag{19}$$

Equations (18) and (19) are used to eliminate the location of point 2 between the relationship of points 1, 2, n, as obtained from equations (10) and (11), therefore the relationship between points 1 and n is found. As the location of the receiving point n is known β'_{jn}, ψ_{jn}, q_{jn}, and $\mathrm{d}A_{jn}/\mathrm{d}A_j$ are evaluated.

2.5. *Special cases*

Two special cases are presented as follows.

2.5.1. *Conical cavity.* Substituting radius $r_p = 0$ into equations (2)–(5), the incident flux of a focused Gaussian distribution on the conical cavity becomes

$$q_j = \frac{3}{2\pi(1-\cos\beta)\{(z_j\tan\phi)^2+[s_0-z_j\,\mathrm{sign}(f+h)]^2\}} \exp\left\{-3\left[\frac{1}{\beta}\tan^{-1}\frac{z_j\tan\phi}{s_0-z_j\,\mathrm{sign}(f+h)}\right]^2\right\}. \tag{20}$$

Replacing ω, $r_p\cos\phi$, and $r_p\cos\phi + z\tan\phi$ in equation (8) by $90°-\phi$, $\eta_j\sin\phi$, and $\eta_i\sin\phi$, respectively, gives a view factor between two parallel rings on the conical cavity as

$$\mathrm{d}F_{\mathrm{d}A_j-\mathrm{d}A_i} = \frac{\cos^2\phi}{2\eta_j\sin\phi}\left\{1-\frac{|\eta_j-\eta_i|[(\eta_i-\eta_j)^2+6\eta_i\eta_j\sin^2\phi]}{[(\eta_i-\eta_j)^2+4\eta_i\eta_j\sin^2\phi]^{3/2}}\right\}\mathrm{d}\eta_i. \tag{21}$$

Replacing the coordinate η_i in equation (21) by η_2 from equation (15), a relationship between η_1, η_n, and η_j is obtained. Furthermore, when η_j and η_i are substituted for η_1 and η_n, respectively, the total view factor from equation (21) leads to

$$\mathrm{d}F_{(\mathrm{d}A_j-\mathrm{d}A_i)_t} = \frac{\cos^2\phi}{2\sin\phi}\sum_{n=2}^{\infty}\rho^{n-2}\left\{1-\left|\frac{C_{n-1}\eta_i}{C_{n-2}\eta_i+\eta_j}-1\right| \times \frac{\left(\frac{C_{n-1}\eta_i}{C_{n-2}\eta_i+\eta_j}-1\right)^2+\frac{6C_{n-1}\eta_i\sin^2\phi}{C_{n-2}\eta_i+\eta_j}}{\left[\left(\frac{C_{n-1}\eta_i}{C_{n-2}\eta_i+\eta_j}-1\right)^2+\frac{4C_{n-1}\eta_i\sin^2\phi}{C_{n-2}\eta_i+\eta_j}\right]^{3/2}}\right\} \cdot\frac{C_{n-1}\eta_j}{(C_{n-2}\eta_i+\eta_j)^2}\mathrm{d}\eta_i. \tag{22}$$

Using equation (18) and (19) the first and second striking points of energy rays emitted from the point source are

$$\eta_2 = D(\eta_1)\eta_1 \tag{23}$$

where the function D is

$$D(\eta_1) = -1+2\cos^2\phi - \sqrt{(1-2\cos^2\phi)^2 - 1 + 4\cos^2\phi\left\{\left(\frac{\eta_1\sin\phi}{s_0}\right)^2 + \left[1-\frac{\eta_1\cos\phi}{s_0}\operatorname{sign}(f+h)\right]^2\right\}}\Big/\left(1-4\cos^2\phi\left\{\left(\frac{\eta_1\sin\phi}{s_0}\right)^2 + \left[1-\frac{\eta_1\cos\phi}{s_0}\operatorname{sign}(f+h)\right]^2\right\}\right). \tag{24}$$

Substituting equation (24) into equation (15) leads to

$$\eta_1 = \frac{[C_{n-1} - C_{n-2}D(\eta_1)]\eta_n}{D(\eta_1)}, \quad n \geqslant 2. \tag{25}$$

Equation (25) indicates that η_1 representing the first impinging point of energy rays emitted from the point source that arrives at η_n with n intervening specular reflections can be determined by fixing η_n so that q_{jn}, ψ_{jn}, β'_{jn} and dA_{jn} relevant to η_1 are found. ψ_j and ψ_{jn} are $90^\circ - \phi$ for cone.

For a collimated incident flux ($\beta \to 0$) the relationship between the locations of the striking point after the first specular reflection by using equation (25) becomes

$$r_2 = \frac{r_1}{4\cos^2\phi - 1}. \tag{26}$$

2.5.2. *Hemispherical cavity.* Setting $z = 0$ in equations (4) and (5) the focused incident flux of a Gaussian distribution yields

$$q_j = \frac{3}{2\pi(1-\cos\beta)\{(r_p\sin\omega_j)^2 + [s_0 - r_p(1-\cos\omega_j)\operatorname{sign}(f+h)]^2\}} \cdot \exp\left\{-3\left[\frac{1}{\beta}\tan^{-1}\frac{r_p\sin\omega_j}{s_0 - r_p(1-\cos\omega_j)\operatorname{sign}(f+h)}\right]^2\right\}. \tag{27}$$

Using equations (4)–(6) the inclination angle of the wall becomes

$$\psi_j = \sin^{-1}\left\{\frac{1}{r_p}\cdot\sqrt{(r_p\sin\omega_j)^2 + [s_0 - r_p(1-\cos\omega_j)\operatorname{sign}(f+h)]^2} \cdot \sin\left[\tan^{-1}\frac{r_p\sin\omega_j}{s_0 - r_p(1-\cos\omega_j)\operatorname{sign}(f+h)}\right]\right\}. \tag{28}$$

The view factor between a ring element in the hemisphere and the point source can be obtained by setting $\phi = 0$ and $z = 0$ in equation (8) giving

$$dF_{dA_j - dA_i} = \frac{dA_i}{4\pi r_p^2}. \tag{29}$$

Combining equations (17) and (29), as mentioned previously, in a conical cavity the total view factor for the hemisphere is given by [33]

$$dF_{(dA_j - dA_i)_t} = \frac{dA_i}{4\pi r_p^2}\sum_{n=2}^{\infty}\frac{\rho_s^{n-2}}{(n-1)^2}, \quad n \geqslant 2. \tag{30}$$

Using equations (18) and (19) the relationship between the first and second striking points of energy rays emitted from the point source is

$$\omega_2 + \omega_1 = \pi - 2[\omega_1 - \beta'_i\operatorname{sign}(f+h)] \tag{31}$$

and

$$\tan\beta'_i = \frac{r_p\sin\omega_1}{s_0 - r_p(1-\cos\omega_1)\operatorname{sign}(f+h)}. \tag{32}$$

By fixing the receiving point ω_n, the angle ω_1 can be determined by substituting equations (31) and (32) into equation (17). As the angle β'_i is known, q_{jn}, ψ_{jn}, β'_{jn}, and dA_{jn} can be found.

2.6. *Numerical method*

An iterative procedure to obtain energy absorption is discussed as follows:

(1) the dimensionless control parameters, f, r_f, β, ϕ, r_c, ρ_s, and ρ_d are specified;
(2) the cavity wall is divided into ring elements;
(3) an initial diffuse radiosity W is guessed;
(4) the incident flux, diffuse irradiation, and specular reflection are evaluated from equations (2), (7) or (8), (10), (15) or (17), (18) and (19), respectively;
(5) an improved W is calculated from equation (1);
(6) steps 4–5 are repeated until W converges.

Convergence of energy absorbed was achieved for ring elements of 100, 150 and 200 within a relative deviation of 10^{-3}.

3. RESULTS AND DISCUSSION

In this work, energy absorbed by the wall of the cavity is governed by the following dimensionless control parameters: the location (f) and the size (r_f) of the focal spot, the convergence angle (2β) of the energy-beam, the cone angle (2ϕ) and cap radius (r_c) of the cavity, specular reflectivity (ρ_s), and absorptivity (α). Given a convergence angle and focal spot location, the focal spot size is chosen to satisfy relevant values of the dimensionless energy distribution parameter of around 1–1.5 on the workpiece surface [11]. Typical values of dimensionless parameters are $r_c = 0.2$, $\phi = 30^\circ$, $f = 0$, $r_f = 1$, $\beta = 0.1$ (radian), $\rho_d = 0.2$, $\rho_s = 0.3$ and $\alpha = 0.5$.

The accuracy of this work is supported by comparison with a theoretical result for the energy absorbed by a hemispherical cavity subject to a col-

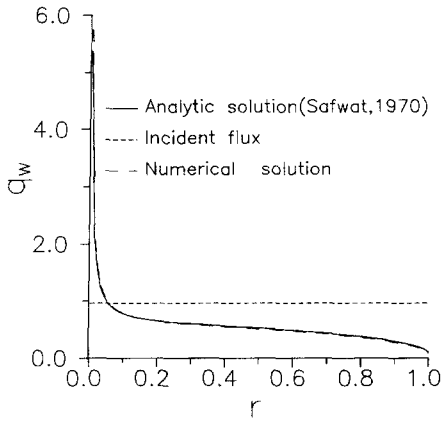

Fig. 4. Comparison of dimensionless absorbed energy per unit area of a hemispherical cavity wall irradiated by collimated uniform beam between this work and analytical result [33].

limated uniform energy-beam [33]. In Fig. 4, the abscissa and ordinate represent the dimensionless radial coordinate and energy flux absorbed by a unit area of the cavity wall, respectively. It is seen that good agreement is achieved. The incident flux per unit area of the cavity opening is also plotted for comparison.

It is crucial to investigate an asymptotic case $s_0 \gg 1$ or $\beta \to 0$ governed by equation (26) which is valid for $r_c \leqslant r_1 \leqslant 1$ and $r_c \leqslant r_2 \leqslant 1$. This indicates that a decrease in the cone angle or increase in the cavity depth results in the striking points of energy rays after the first specular reflections to be lower in the cavity. Substituting radius $r_1 = 1$ into equation (26) the radius of the striking point $r_2 = 1/(4\cos^2\phi - 1) \equiv r_s$. For a half cone angle equal to or greater than 60°, the critical radius $r_s \to \infty$ or becomes negative, which indicates that no specular reflection impinges on the cavity wall. All energy rays after striking the cavity wall escape through the cavity opening to the surroundings, as illustrated in Fig. 5(a). A further decrease in half cone angle to $45° \leqslant \phi \leqslant 60°$ also causes incident rays in the region $r_1 > 4\cos^2\phi - 1$ to escape to the surroundings after the first specular reflections, as illustrated in Fig. 5(b). For an incident ray between $r_c \leqslant r_1 \leqslant 4\cos^2\phi - 1$ energy rays after the first specular reflection strike the cavity wall on the other side at a higher location. All energy rays after the first specular reflections are directed upwards. As a result, the spherical cap does not experience first specular reflections.

For a half cone angle in the range $0 \leqslant \phi \leqslant 45°$ the first specular reflected rays of incident fluxes between $r_c(4\cos^2\phi - 1) \leqslant r_1 \leqslant 1$ and $r_c \leqslant r_1 \leqslant r_c(4\cos^2\phi - 1)$ impinge on the conical wall and spherical cap, respectively. The reflected rays are in downward directions. Therefore, it is not possible for energy rays after the first specular reflections to impinge on locations with radii $r_2 > r_s$, as illustrated in Fig. 5(c). Multiple specular reflections from direct incident rays and reflected rays take place in the spherical cap. A large radius of the curvature for the spherical cap also increases the

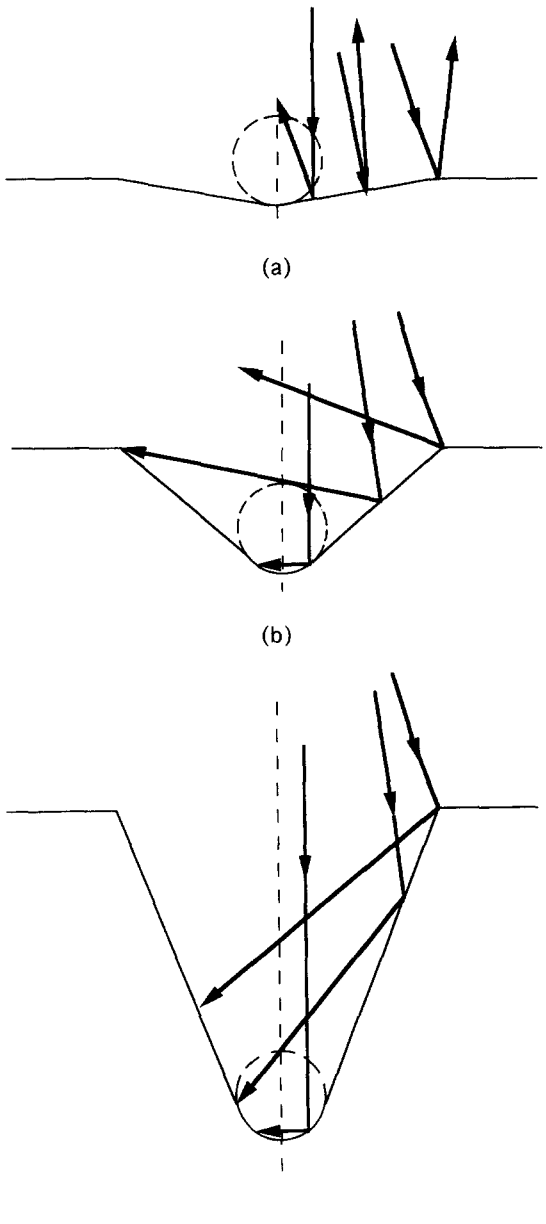

Fig. 5. Sketch indicating the first specular reflection on cavity of (a) large cone angle; (b) intermediate cone angle; (c) small cone angle.

number of specular reflections. Energy rays after the first specular reflections cannot reach the bottom of the spherical cap if the following relation

$$\phi \geqslant \frac{1}{3}\left[90° - 2\,\mathrm{sign}(f+h)\tan^{-1}\cdot\frac{r_c}{s_0 - (r_p - \sqrt{r_p^2 - r_c^2})\,\mathrm{sign}(f+h)}\right] \quad (33)$$

which is obtained from equations (18) and (19), is satisfied.

The effects of the cone angle on energy absorption

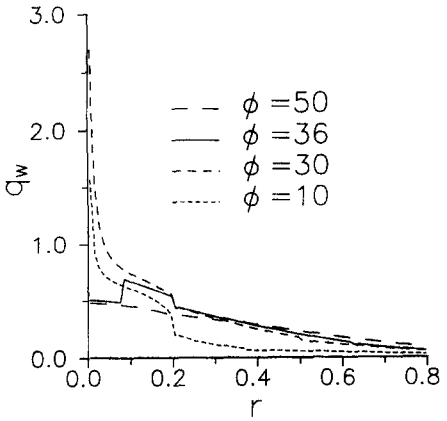

Fig. 6. Distribution of dimensionless absorbed energy per unit area of the cavity wall for different half cone angles.

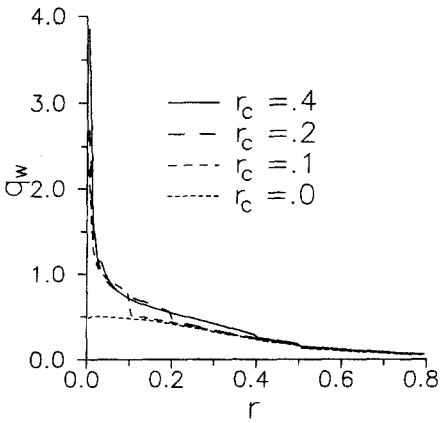

Fig. 7. Distribution of dimensionless absorbed energy per unit area of the cavity wall for different radii of spherical cap.

are shown in Fig. 6. It can be seen that for the half cone angle $\phi = 50°$ energy absorbed near the cavity base is low. This is attributed to upward directions of energy rays after the first specular reflections by the conical wall. A slight increase of absorption exists at a radius of 0.332 because the second specular reflections take place for $r_2 > r_c/(4\cos^2\phi - 1)$ (see Fig. 5(b)). Even though the half cone angle is 36°, in which the first specular reflections are downward, energy absorbed near the axisymmetric axis is low. This is because energy rays after the first specular reflections cannot impinge on the spherical cap for $r_2 < 0.1$ (see Fig. 5(c)). A jump at r equal to 0.1 and a drop at 0.2 results from receiving energy rays after the first specular reflections and having distinct curvatures between the conical wall and spherical cap, respectively. A significant increase in absorption near the axisymmetric axis occurs for half cone angles of 10 and 30°. This is because the entire spherical cap can receive energy rays after the first specular reflections. Absorption for the half cone angle of 10° is higher than that of 30°. The reason for this is that a large cone angle indicates a shallow cavity and an increase in intensity of incident fluxes on the wall.

Energy absorbed for different radii of spherical caps is shown in Fig. 7. For a conical cavity having a zero radius of the spherical cap, the energy absorbed exhibits a decrease near the axisymmetric axis and at a radius of 0.5, respectively. Substituting a half cone angle $\phi = 30°$ and $r_1 = 1$ into equation (26) gives $r_2 = 0.5$. Therefore, the region for radii greater than 0.5 does not experience energy rays after the first specular reflection. The decrease in absorption near the axisymmetric axis is a result of a reduction in diffuse reflection. As the spherical cap increases in radius absorption increases rapidly near the axisymmetric axis or spherical cap. The increase of absorption in the spherical cap is attributed to not only direct irradiation of incident rays and their specular reflections, but also all irradiation in the range $r_c \leqslant r \leqslant r_c(4\cos^2\phi - 1)$ after the first specular reflection, and multiple reflections from other regions of the cavity wall (see Fig. 5(c)). For $r_c = 0.1$, 0.2 and 0.4 drops at radii $r = 0.1$, 0.2 and 0.4, respectively, are evidently due to distinct curvatures at the intersections of the conical surface and spherical cap.

During welding a shaped cavity can be produced. This study finds that as the cavity becomes sharper energy absorption near the cavity base is reduced. In view of surface tension the free surface of the cavity base becomes spherical. Absorption near the base thus increases and induces a V-shaped cavity again. The process is repeated and spiking results. Konkol *et al.* [3] observed that spiking always occurred with a V-shaped cavity.

Figure 8 shows that the effect of focal location on energy absorption. Dimensionless focal locations of 0 and 5 represent the focal spot lying above the cavity base having a dimensionless depth of 1.5. The incident fluxes can be considered as emitted from virtual point sources with dimensionless distances $s_0 = 11.5$ and 16.5, respectively. As a result, the intensity of the incident flux and absorbed energy for the latter are smaller than the former. For a focal location of -3 the focal spot is below the cavity base. The incident flux can be considered as emitted from an imaged

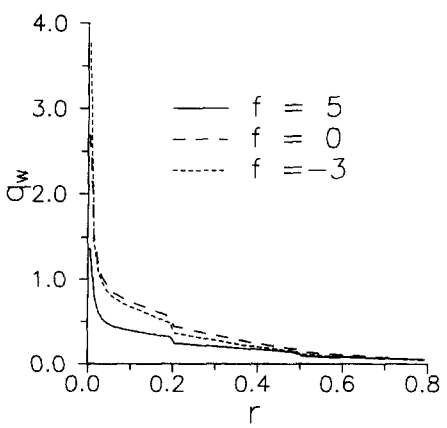

Fig. 8. Distribution of dimensionless absorbed energy per unit area of the cavity wall for different focal locations.

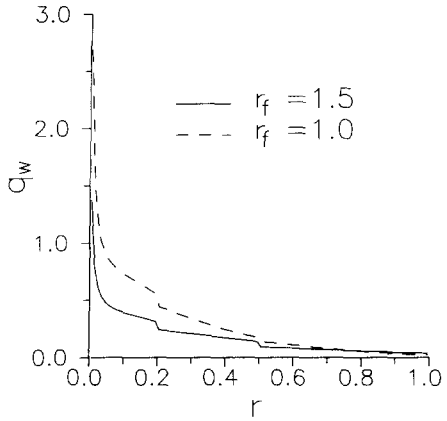

Fig. 9. Distribution of dimensionless absorbed energy per unit area of the cavity wall for different sizes of the focal spot.

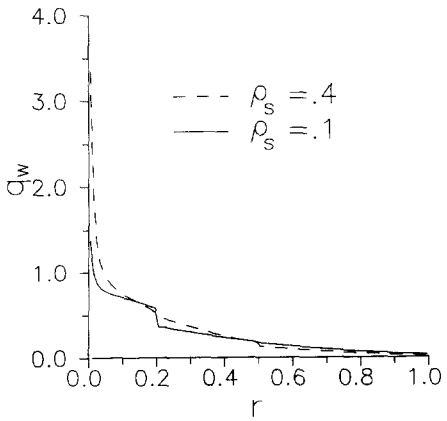

Fig. 11. Distribution of dimensionless absorbed energy per unit area of the cavity wall for different specular reflectivities.

point source below the cavity base. Absorption near the cavity base therefore is enhanced due to not only a decrease in the distance between the cavity base and imaged point source, but also the downward direction of energy rays after their first specular reflections. The focusing effect therefore is more pronounced for the focal spot below the cavity base. In view of a change in the focal location from above (or below) to below (or above) the cavity base results indicate that spiking readily occurs.

The effect of the focal spot size on energy absorption is presented in Fig. 9. A large size of the focal spot implies a large distance between the virtual or imaged point source and cavity base. As a consequence, intensity of irradiation on the cavity wall is reduced. A small convergence angle induces high intensity energy ray. As a result, absorption is enhanced, as shown in Fig. 10.

Distributions of energy absorbed by cavity walls for different specular or diffuse reflectivities are shown in Fig. 11. It can be seen that a large specular reflectivity enhances energy absorption near the axisymmetric axis and slightly increases the jump at r_2 ($= 0.5$). Furthermore, the absorbed energy flux for $\rho_s = 0.1$ is higher than that of $\rho_s = 0.4$ in the regions $0.14 < r < 0.2$ and $r > r_s$. This is because of diffuse irradiation.

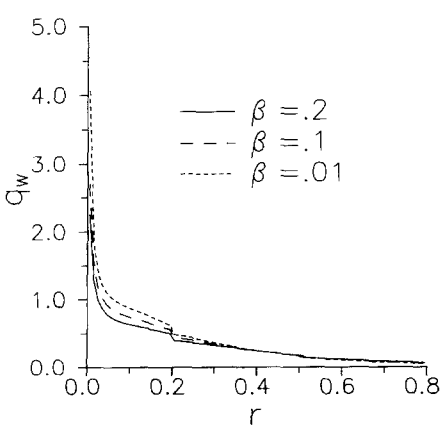

Fig. 10. Distribution of dimensionless absorbed energy per unit area of the cavity wall for different half convergence angles.

4. CONCLUSIONS

The following conclusions are drawn:

(1) Energy absorbed by a conical cavity truncated by a spherical cap exhibits different behavior for different cone angles. For a large half cone angle (e.g. $\phi \geqslant 60°, \beta \to 0$) or a shallow cavity energy absorption is uniformly low. This is because all energy rays after the first specular reflections escape to the surroundings. A decrease in the half cone angle ($45° \leqslant \phi \leqslant 60°$) slightly increases absorption near the cavity base. A slight jump as a result of receiving energy rays after the first specular reflections is seen. A further decrease in the cone angle, however, exhibits a jump and a drop from receiving energy rays after the first specular reflections and distinct curvatures between the conical wall and spherical cap, respectively. A rapid increase in absorption occurs near the axisymmetric axis or spherical cap for a small cone angle.

(2) An increase in the radius of the spherical cap enhances energy absorption near the cavity base. The increase of absorption in the spherical cap is attributed to not only direct irradiation of incident rays and their specular reflections, but also all irradiation from the conical wall after the first specular reflection, and multiple reflections from other regions of the cavity wall.

(3) Energy absorption is enhanced as the focal spot approaches the cavity base in the downward direction. For the same distance between the focal spot and the cavity base, energy absorbed for the focal spot below the cavity base is higher than that above the cavity base near the axisymmetric axis.

(4) Energy absorbed is reduced by increasing the convergence angle and focal spot size in the conical cavity with a spherical cap.

(5) Spiking in welding is proposed to be the result

of changes in either the curvature of the cavity base, or the location of the focal spot from the above (or below) to below (or above) the cavity base.

Acknowledgements—The authors acknowledge the interest and guidance of Professor W. H. Giedt and the financial support from the National Science Council, Taiwan, Republic of China, under the grant number NSC 85-2212-E-110-017.

REFERENCES

1. Keanini, R. G. and Rubinsky, B., Plasma arc welding under normal and zero gravity. *Welding Journal*, 1990, **69,** 41–49.
2. Giedt, W. H. and Tallerico, L. N., Prediction of electron-beam depth of penetration. *Welding Journal*, 1988, **67,** 299s–305s.
3. Konkol, P. J., Smith, P. M., Willebrand, C. F. and Connor, L. P., Parameter study of electron-beam welding. *Welding Journal*, 1971, **50,** 765s–776s.
4. Armstrong, R. E., Control of spiking in partial penetration electron beam welds. *Welding Journal*, 1970, **49,** 382s–388s.
5. Giedt, W. H., A periodic melting model of high intensity electron beam welding. In *Modeling of Casting, Welding, and Advanced Solidification Processes—V*, ed. M. Rappaz, M. R. Özgü, K. Mahin, and W. Davos. TMMMS, Warrendale, PA, 1991, pp. 115–122.
6. Schiller, S., Heisig, U. and Panzer, S., *Electron Beam Technology*, Wiley, New York, 1982, p. 317.
7. Irie, H., Tsukamoto, S. and Inagaki, M., Relation between beam properties and shape of fusion zone in electron beam welding (Report 1). *Journal of the Japan Welding Society*, 1982, **51,** 941–945 (in Japanese).
8. Adams, M. J., Low voltage electron beam welding : effect of process parameters. *British Welding Journal*, 1968, **15,** 134–142.
9. Adams, M. J., High voltage electron beam welding-effect of process parameters. *British Welding Journal*, 1968, **15,** 451–467.
10. Engquist, R. D., Parameters affecting electron beam welding. *Metals Engineering Quarterly*, 1968, **8,** 56–63.
11. Wei, P. S. and Chow, Y. T., Beam focusing characteristics and alloying element effects on high-intensity electron beam welding. *Metallurgical Transactions B*, 1992, **23B,** 81–90.
12. Arata, Y., *Plasma, Electron and Laser Beam Technology*. American Society for Metals, Metals Park, Ohio, 1986, pp. 217–225.
13. Siegel, R. and Howell, J. R., *Thermal Radiation Heat Transfer*, Chap. 11. McGraw-Hill, New York, 1972.
14. Modest, M. F., *Radiative Heat Transfer*, Chap. 19. McGraw-Hill, New York, 1993.
15. Toor, J. S. and Viskanta, R., A numerical experiment of radiant heat interchange by the Monte-Carlo method. *International Journal of Heat and Mass Transfer*, 1968, **11,** 883–897.
16. Howell, J. R., *Advances in Heat Transfer*, (ed. T. F. Irvine, Jr and J. P. Hartnett), Vol. 5. Academic Press, New York, 1968, pp. 1–54.
17. Wang, S. C. and Wei, P. S., Energy-beam redistribution and absorption in a drilling or welding cavity. *Metallurgical Transactions B*, 1992, **23B,** 505–511.
18. Hicken, G. K., Giedt, W. H. and Bentley, A. E., Correlation of joint penetration with electron beam current distribution. *Welding Journal*, 1991, **70,** 69s–75s.
19. Wei, P. S., Wu, T. H. and Chow, Y. T., Investigation of high-intensity beam characteristics on welding cavity shape and temperature distribution. *ASME Journal of Heat Transfer*, 1990, **112,** 163–169.
20. Schauer, D. A. and Giedt, W. H., Prediction of electron beam welding spiking tendency. *Welding Journal*, 1978, **57,** 189s–195s.
21. von Allmen, M., Laser drilling velocity in metals. *Journal of Applied Physics*, 1976, **47,** 5460–5463.
22. Miyazaki, T., Material removal produced by a high-power-density electron beam. *Journal of Applied Physics*, 1977, **48,** 3035–3041.
23. Poueyo-Verwaerde, A., Fabbro, R., Deshors, G., de Frutos, A. M. and Orza, J. M., Experimental study of laser-induced plasma in welding conditions with continuous CO_2 laser. *Journal of Applied Physics*, 1993, **74,** 5773–5780.
24. Collur, M. M. and DebRoy, T., Emission spectroscopy of plasma during laser welding of AISI 201 stainless steel. *Metallurgical Transactions B*, 1989, **20B,** 277–286.
25. Zel'dovich, B. Ya. and Raizer, Yu. P., *Physics of Shock Waves and High-Temperature Hydrodynamic Phenomena*, Chapter V, Vol. 1. Academic Press, New York, 1966.
26. Shui, V. H., Kivel, B. and Weyl, G. M., Effect of vapor plasma on the coupling of laser radiation with aluminum targets. *Journal of Quantitative Spectroscopy and Radiative Transfer*, 1978, **20,** 627–636.
27. Matsunawa, A. and Ohnawa, T., Beam–plume interaction in laser materials processing. *Transactions of Japan Welding Research Institute*, 1991, **20,** 9–15.
28. Matsunawa, A., Yoshida, H. and Katayama, S., Beam–plume interaction in pulsed YAG laser processing. In *Proceedings of the Materials Processing Symposium*, Vol. 44, *The International Conference on Applications of Lasers and Electro-optics* (ICALEO'84), ed. J. Mazumder. Boston, 1984, pp. 35–42.
29. Duley, W. W., A comparison of keyhole absorption processes in laser and electron beam welding. *Proceedings of the Conference on the Laser vs the Electron Beam in Welding, Cutting and Surface Treatment—State of the Art*—1987, ed. R. Bakish. Bakish Materials Corp., Englewood, NJ, 1987, pp. 160–167.
30. Miyamoto, I., Maruo, H. and Arata, Y., The role of assist gas in CO_2 laser welding. In *Proceedings of the Materials Processing Symposium, The International Conference on Applications of Lasers and Electro-optics* (ICALEO'84), Vol. 44, ed. J. Mazumder. Boston, 1984, pp. 68–75.
31. Stevenson, J. A. and Grafton, J. C., Radiation heat transfer analysis for space vehicles. ASD Technical report 61-119, Part I, North American Aviation, Inc. for Aeronautical Systems Division, AFSD, US Air Force, Wright Patterson AFB, Ohio, 1961.
32. Lin, S. H. and Sparrow, E. M., Radiant interchange among curved specularly reflecting surfaces—application to cylindrical and conical cavities. *ASME Journal of Heat Transfer*, 1965, **87,** 299–308.
33. Safwat, H. H., Absorption of thermal radiation in a hemispherical cavity. *ASME Journal of Heat Transfer*, 1970, **92,** 198–201.